Early summer hydroclimatic signals were well captured by tree-ring earlywood width in the eastern Qinling Mountains (central China)

Yesi Zhao[1,2], Jiangfeng Shi[1,3], Shiyuan Shi[1], Xiaoqi Ma[1], Weijie Zhang[1], Bowen Wang[1], Xuguang Sun[4], Huayu Lu[1], Achim Bräuning[2]

[1] School of Geography and Ocean Science, Nanjing University, Nanjing 210023, China
[2] Institute of Geography, Friedrich-Alexander-University Erlangen-Nürnberg, Erlangen 91058, Germany
[3] Laboratory of Tree-Ring Research, University of Arizona, Tucson 85721, USA
[4] School of Atmospheric Sciences, Nanjing University, Nanjing 210023, China

Correspondence to: Jiangfeng Shi (shijf@nju.edu.cn)

Abstract. Tree-ring width (TRW) chronologies could only provide limited amount of moisture-related climatic information in the humid and semi-humid regions of China; thus, it is worth to explore the potentials of the intra-annul tree-ring width indices (i.e., the earlywood width (EWW) and latewood width (LWW)) to provide some additional climatic information. To fulfill this task, TRW, EWW and LWW were measured from the tree-ring samples of *Pinus tabulaeformis* in a semi-humid region, that is, the eastern Qinling Mountains, Central China. Their standard (STD) and signal-free (SSF) chronologies were created using different detrending methods including (1) negative exponential function together with linear regression with negative (or zero) slope (NELR), (2) cubic smoothed splines with a 50% frequency cutoff of 67% of the series length (SP67), and (3) age-dependent splines with an initial stiffness of 50 years (SPA50). The results showed that EWW chronologies were significantly negatively correlated with temperature, but positively correlated with precipitation and soil moisture conditions during the current early growing season. Comparatively, LWW and TRW chronologies had weaker relationships with these climatic factors. EWW STD chronology with the detrending method of NELR contained the strongest climatic signal, explaining 50% variance of the May–July self-calibrated Palmer Drought Severity Index (MJJ scPDSI) during the instrumental period 1953–2005. Based on this relationship, the MJJ scPDSI was reconstructed using a linear regression function with strong statistical parameters over the period 1864–2005, and the reconstruction was further validated by comparing with other hydroclimatic reconstructions and historical document records in adjacent regions. On the decadal and longer time scales, a stable relationship between the reconstructed MJJ scPDSI and the East Asian Summer Monsoon index (EASMI) only existed until the 1940s, partly because the study region is outside of the mei-yu/changma/baiu rainband where the influence of EASM on precipitation is supposed to be stable. The climatic potential of intra-annual tree-ring indices might be explored in the future at other sites in humid and semi-humid regions.

1. Introduction

Most of the existing tree-ring width (TRW) based hydroclimatic reconstructions have fallen in the regions between the 200-to 600-mm annual precipitation isolines in China (Liu et al., 2018b), close to the northern fringe of Asian Summer Monsoon. Comparatively, there are still a small amount of hydroclimatic reconstructions in the core monsoon region, for example, a few

5 case studies in Southeast China (e.g. Cai et al., 2017; Chen et al., 2016a; Shi et al., 2015), North China (e.g. Chen et al., 2016b; Hughes et al., 1994; Lei et al., 2014; Liu et al., 2002), and the Hengduan mountains in Southwest China (Fan et al., 2008; Fang et al., 2010; Gou et al., 2013; Li et al., 2016). Since precipitation is spatially variable (Ding et al., 2013), hdyroclimatic variations in the monsoon fringe can not completely represent those in the core monsoon region (Liu et al., 2018b). Thus, more hydroclimatic reconstructions are needed in the monsoon region.

10 Some TRW chronologies within the monsoon region showed weak or unstable hydroclimatic signals (e.g. Li et al., 2016; Shi et al., 2012; Wang et al., 2018), unable to be used for reliable reconstruction. Intra-annually resolved tree-ring width (i.e., earlywood width (EWW) and latewood width (LWW)), however, provided stronger hydroclimatic signals than TRW in some cases (Chen et al., 2012; Zhao et al., 2017 a, b). This might be related to the seasonal movement of monsoon rainbelt which causes water restrictions on tree growth during parts of the growing season (Liu et al., 2018a).

15 The eastern Qinling Mountains are located within the core region of East Asian Summer Monsoon (EASM), and are characterized by a transitional climate from warm-temperate to subtropical. In this region, Shi et al. (2012) has built four TRW chronologies of *Pinus tabulaeformis* along an elevation gradient in Mount Funiu. The TRW chronologies from the two low-altitude sites, Baiyunshan (BYS) and Longchiman (LCM), exhibited a positive response to precipitation and negative response to temperature during early summer, showing some kind of water stress. However, the dendroclimatic potentials of EWW and

20 LWW were not explored. Meanwhile, tree-growth at an adjacent site was more restricted by the drought index, PDSI (Palmer Drought Severity Index), than precipitation and temperature (Peng et al. 2014), indicating that this parameter should also be incorporated into the analysis. In addition, Zhao et al. (2015) proposed a new East Asian Summer Monsoon index (EASMI), which shows a good performance in describing summer climate variability over East Asia. This allows us to study the response of local hydroclimate to EASM with these tree-ring materials and the newly proposed EASMI.

25 Since the TRW of *P. tabulaeformis* in BYS and LCM were mainly restricted by the early summer moisture condition, we hypothesize that the early summer hydroclimatic signals might be strengthened only using EWW, with the exclusion of LWW from TRW. Therefore, the objectives of this study are (1) to verify that EWW is more sensitive to early summer hydroclimatic factors than TRW and LWW for *P. tabulaeformis* at BYS and LCM, (2) to reconstruct early summer hydroclimate variations using EWW, and (3) to tentatively explore the relationship between the reconstructed hydroclimate variability and EASM.

2. Materials and Methods

2.1. Study sites

Dated tree-ring samples of *P. tabulaeformis* used in this study were provided by Shi et al. (2012). They were collected from two sampling sites in Mount Funiu in 2006 and 2008 separately: BYS (33.63° N, 111.85° E) and LCM (33.68° N, 112.05° E) (Fig. 1). The sampling sites were located on mountain tops, where soils are thin and well-drained. The elevations of BYS and LCM range from 1200–1300 m above sea level (asl), and 1340–1400 m asl, respectively. The regional annual mean temperature and annual total precipitation are 14.1 °C and 822 mm, respectively. The majority part of the annual total precipitation drops during the warm season (Fig. 2). More detailed information of the study sites can be found in Shi et al. (2012).

2.2 Tree-ring data

The selected *P. tabulaeformis* is a widely distributed conifer species in North China with the extension from 31° 00′ N to 43° 33′ N, and 103° 20′ E to 124° 45′ E (Xu et al., 1981). Liang et al. (2009) studied the cambial dynamics of *P. tabulaeformis* in its northern distribution limit (43° 14' N, 116° 24' E, 1363 m a.s.l.), and found that the cell division in the cambial zone started within the third week of May and did not complete aroud mid-Septermber. Zeng et al. (2018) found that the cambial cells of mature *P. tabulaeformis* in Northwest China (37° 02′ N, 104° 28′ E, 2456 m a.s.l.) started in late spring and ceased in late July to early August. Considering that our sampling sites are located at lower latitudes, the cambial activites of *P. tabulaeformis* in our study may start earlier and ends later than those found in above studies according to the temperature-controlled phenology theory (Chen and Xu, 2012).

P. tabulaeformis generally exhibits an abrupt transition from light-colored earlywood to dark-colored latewood (Liang and Eckstein, 2006; Fig. S1), and the transition can occur in mid-July in Beijing (39.9° N, 116.3° E) (Zhang et al., 1982). Due to this wood anatomical characteristic, the earlywood and latewood segments of annual growth rings can be discriminated visually by the sudden change in cell size, lumen size, and color (Stahle et al., 2009). However, gradual transitions also occur in a few samples, making the earlywood-latewood boundary difficult to discern. Therefore, only samples with distinct earlywood and latewood segments were used for subsequent measurements (Knapp et al., 2016). In total, 20 cores from 11 trees and 42 cores from 22 trees were selected from BYS and LCM, respectively. EWW and LWW were then measured using a LINTAB5 system at a resolution of 0.001 mm, and TRW was obtained by adding EWW and LWW together.

2.3 Development of tree-ring width chronologies

Non-climatic growth trends need to be fitted and removed from each "raw" (untreated) EWW, LWW and TRW series, which is known as detrending (Cook et al., 1990). In order to check the effects of detrending methods on the preservation of climatic signals, three detrending methods were selected for comparison. They were negative exponential function together with linear regression with negative (or zero) slope (NELR), cubic smoothed splines with a 50 % frequency cutoff of 67 % of the series length (SP67), and age-dependent splines with an initial stiffness of 50 years (SPA50). NELR is a deterministic method based

3

on the assumption that tree radial growth declines monotonically (Cook et al., 1990). SP67 has a good ability in fitting the potential low-and middle-frequency perturbations contained in ring-width series (Cook et al., 1990). It allows no more than half of the amplitude of variations with wavelength of two-thirds of the length of series being preserved in resulting indices (Melvin et al., 2007). SPA50 specifies annually varying 50 % frequency cutoff parameter for each year by adding the initial stiffness with ring age. In comparison with SP67, it makes the resulting spline become more flexible in the early years and progressively stiffer in later years (Melvin et al., 2007). All raw ring-width series were divided by the estimated growth trends, and the resulting detrended ring-width series were averaged to generate the standard (STD) chronologies using the bi-weight robust mean method (Fig. S2). Since the traditional fitted curves may contain the climatic signals, which is termed as "trend distortion" problem (Melvin and Briffa, 2008), the signal-free (SSF) method is introduced to create the fitted growth curve free of climatic signals by dividing the raw ring-width series by the STD chronology via iterations (Melvin and Briffa, 2008). Therefore, the SSF chronologies were also developed for analysis (Fig. S3). The variance of each chronology was stabilized to minimize the effects of sampling depth according to the methods described in Osborn (1997). The temporal extension for all width chronologies in BYS and LCM are 1841–2005 and 1850–2005, respectively. EPS (expressed population signal) and Rbar calculated over 51-year windows were used to evaluate the quality of the width chronologies (Cook et al., 1999; Wigley et al., 1984). Rbar represents the mean of all correlations for ring-width series between each pair of cores. EPS is a function of Rbar and sample size, and is used to estimate how well the sample chronology represents the theoretical chronology. The reliable period for each chronology is determined based on the generally accepted EPS threshold value of 0.85 (Wigley et al., 1984). All above processes were performed with the program RCSsigFree Version 45_v2b (http://www.ldeo.columbia.edu/tree-ring-laboratory/resources/software).

The with chronologies from the two sampling sites show high degree of coherence as evidenced by their significant positive correlations ($p < 0.001$) during their common period when EPS larger than 0.85 (Table S1). Moreover, the positive correlations remain significant ($p < 0.001$) after removing the influence of autocorrelations and linear trends (Table S1). This indicates that the two sites share common climatic signals. Therefore, we pooled all raw ring-width series from the two sites, and developed composite STD and SSF chronologies for EWW, LWW and TRW using the three detrending methods as described above (Fig. S4). Statistics for each chronology including the starting year when EPS larger than 0.85, standard deviation, mean sensitivity and first-order correlation coefficient (AR1) are shown in Table S3. In addition, several statistics were calculated to assess the degree of similarity among detrended ring-width series over the common period 1915–2005 (Table S4). These statistics are first principial componet (PC1), Rbar, siganl-to-noise ratio (SNR), and EPS (Cook et al., 1990).

2.4. Climate data

Monthly mean maximum (Tmax), minimum (Tmin) and mean temperature (Tmean), and monthly total precipitation (Pre) were selected from four nearby meteorological stations (Table 1; Fig. 1b). These climate data were obtained from the China Meteorological Administration. Regional temperature values were calculated by directly averaging the temperature time series from the four statioins over their common period 1957–2005. Regional precipitation were produced by firstly deriving the

regional averages in terms of percentages, then multiplying the regional mean to transform the resulting series back to millimetre units (Jones and Hulme, 1996). The self-calibrated PDSI (scPDSI) and SPEI were also chosen as the hydroclimatic factors. The PDSI monitors the cumulative departure in surface water balance in terms of moisture supply (precipitation) and demand (potential evapotranspiration) (Palmer, 1965). Here we used the scPDSI instead of PDSI because it has solved the PDSI problems in spatial comparisons by automatically adjusting the climatic characteristic and calculating the duration factors based on the characteristics of the climate at a given location (Wells et al., 2004). The regional scPDSI were calculated by averaging the CRU (Climate Research Unit) scPDSI grids (van der Schrier et al., 2013) over the area between 32° N to 34.5° N and 111° E to 112° E (Fig. 1) where the meteorological stations utilized by CRU dataset were concentrated (Fig. S5; Table S6). The SPEI represents a simple climatic water balance as the form of difference between precipitation and potential evapotranspiration, and can be calculated on different timescales (Vicente-Serrano et al., 2010). We calculated the regional SPEI at three timescales (1-month, 3-month and 12-month) in program R using the "SPEI" package with the climatic factors including regional Tmax, Tmin and Pre (Beguería and Vicente-Serrano, 2012).

In order to validate the reconstruction, we compared the reconstruction with several hydroclimate reconstructions and historical document records (Table 2), including (1) the June–August PDSI from the No. 370 grid point of the Monsoon Asia Drought Atlas (MADA) at 33.75° N, 111.25° E over the period 1864–2005 (PDSI$_{Cook}$; Cook et al., 2010), (2) the dryness/wetness index (DWI) from the grid point at 33.75° N, 111.25° E over the period 1864–2000 (DWI$_{Yang}$; Yang et al., 2013b), (3) reconstructed April–June precipitation based on TRW in Mount Hua over the period 1864–2005 (Pre$_{Chen}$; Chen et al., 2016b), and (4) drought/wet events recorded in historical documents over the period 1864–2005 (Wen, 2006; He, 1980). The DWI dataset were reconstructed from the historical documents and modern instrumental May–September precipitation in 120 sites over China (Chinese Academy of Meteorological Sciences, 1981). The dataset classified the degree of dryness and wetness into five grades: very wet (grade 1), wet (grade 2), normal (grade 3), dry (grade 4), and very dry (grade 5). Yang et al. (2013b) has interpolated the DWI dataset into 2.5° latitude/longitude grid cells.

The EASM circulation was represented by a newly defined East Asian Summer Monsoon index (EASMI) which was developed by Zhao et al. (2015) based on the 200 hPa zonal wind anomalies. It was computed as:

$$EASMI = Nor\,[u(2.5°\!-10°\,N, 105°\!-140°\,E) - u(17.5°\!-22.5°\,N, 105°\!-140°\,E) + u(30°\!-37.5°\,N, 105°\!-140°\,E)] \quad (2)$$

where Nor and u represent standardization and mean 200 hPa zonal wind, respectively. We selected this EASMI is because: (1) it can capture the leading mode of EASM precipitation, whose center is located at the mei-yu–changma–baiu rainband (27.5°–32.5° N, 105°–120° E and 30°–37.5° N, 127.5°–150° E) and the tropical Philippine Sea rainband (10°–20° N, 115°–150° E); (2) it uses the 200 hPa wind filed which was less affected by complex weather processes near the surface; and (3) it can better capture the summer precipitation and temperature characteristics over East Asia compared with previous EASM indices (Zhao et al., 2015). To understand the connections of local precipitation (32°–34.5° N and 111°–112° E) with scPDSI and EASMI, the precipitation data were extracted from the gridded precipitation dataset Global Precipitation Climatology Centre Version 7 (GPCC v7; Schneider et al., 2015). The gridded dataset can represent the variations of precipitation over East China during the 20th century (Wang and Wang, 2017).

5

2.5 Statistical methods

To investigate the climate response of different tree-ring parameters (EWW, LWW, and TRW), we firstly calculated the Pearson correlation coefficients of the STD and SSF tree-ring width chronologies with monthly climate time series. The time window for the correlation analysis spanned from January of two years earlier to October of the current year. Secondly, correlations were calculated between the prewhitened and linearly detrended chronologies and climate time series to evaluate the possible effects of autocorrelations and secular trends. The prewhitening procedure was run with the "ar" funtion in R package "stats". The appropriate autoregressive order was automatically determined by the Akaike Information Criterion (Akaike, 1974). The linear detrending procedure was performed in Matlab with the "detrend" function. Then, we analyzed the response of different tree-ring parameters to multi-month averaged scPDSI (which had the stronger impacts on tree-growth than other climatic factors; see the results for detail) to find the strongest climate-growth relationship. Finally, we used the wavelet coherence method (Grinsted et al., 2004) to test the temporal stability and possible lags of the climate-growth relationship on different frequency domain.

A simple linear regression model was applied to establish the transfer function using May–July (MJJ) scPDSI as the predictant, and the NELR based EWW STD chronology as the predictor (which had the strongest relationship; see the results for detail) over the period 1953–2005. Temporal stability of the model was tested by splitting the MJJ scPDSI into two sub-periods (1953–1979 and 1979–2005) for calibration and verification using the following statistics: correlation coefficient (r), explained variance (R^2), reduction of error (RE), coefficient of efficiency (CE), and the sign-test (Meko and Graybill, 1995). Meanwhile, the possible autocorrelation and trend contained in the regression residuals were evaluated using the Durbin-Watson test (DW; Durbin and Watson, 1950) with the R package "Lmtest", and the two-sided Cox and Stuart trend test (CS; Cox and Stuart, 1955) with the R package "snpar", respectively. A DW value of 2 means no first order autocorrelation in the residuals, whereas values larger (less) than 2 are indicative for negative (positive) autocorrelation. The DW test has the null hypothesis that the autocorrelation of the residuals is 0. The two-sided CS trend test has the null hypothesis that there is no monotonic trend in the residuals. The variance of the MJJ scPDSI reconstruction were restored to match the variance of instrumental MJJ scPDSI during the calibration period using Eq. (1),

$$\text{Adj\_Rec}_i = \frac{(\text{Rec}_i - \overline{\text{Rec}_{cal}})}{\sigma(\text{Rec}_{cal})} \times \sigma(\text{Ins}_{cal}) + \overline{\text{Ins}_{cal}} \qquad (1)$$

where, the Rec_i and Adj_Rec_i indicate the reconstructed value and variance adjusted value for a specific year i. The $\overline{\text{Rec}_{cal}}$ and $\overline{\text{Ins}_{cal}}$ indicate the arithmetic mean of the reconstructed and instrumental values during the calibration period (it is 1953–2005 in this study). The $\sigma(\text{Rec}_{cal})$ and $\sigma(\text{Ins}_{cal})$ are the corresponding standard deviations.

Spatial correlations were calculated between the reconstructed MJJ scPDSI and CRU scPDSI 3.25 dataset (van der Schrier et al., 2013) using the KNMI Climate Explorer (http://climexp.knmi.nl/start.cgi) to investigate the spatial representativeness of our reconstruction. All the hydroclimatic reconstructions were divided into interannual (< 10 years), and decadal and longer-term components (> 10 years) for comparison, respectively. The decadal and longer components were derived by lowpass filtering the original reconstructions using the the adaptive 10 point "Butterworth" low-pass filter at 0.1 cut-off frequency

6

(Mann, 2008). Then, the interannual components were obtained by subtracting the decadal and longer-term components from the original reconstructions. The low-pass filtering technique has a good ability in preserving trends near time series boundaries (Mann, 2008).

We calculated the MJJ EASMI according to the definition of Zhao et al. (2015) using the 200 hPa zonal wind dataset which were obtained from the National Oceanic and Atmospheric Administration-Cooperative Institute for Research in Environmental Sciences (NOAA/CIRES) Twentieth Century Reanalysis V2c (NOAA-20C; Compo et al., 2011) over the period 1864–2005. The relationship between EASMI and our reconstruction was firstly evaluated using the wavelet coherence method (Grinsted et al., 2004). In addition, 21-year moving window correlation analyses were calculated between the decadal-filtered MJJ EASMI, reconstructed scPDSI, and local precipitation to explore the connections of precipitation with scPDSI and EASMI. Moreover, empirical orthogonal function (EOF) analysis and spatial correlation analysis were performed to manifest the impacts of the changed leading EASM mode on the relationship between decadal-filtered EASMI and local precipitation. The filtering procedure was conducted using the "Butterworth" low-pass filter (Mann, 2008) as mentioned above. The filtering, EOF and correlation analyses were performed in Matlab and the plots were drawn with Surfer 10.

The significance tests for all observed correlation coefficients were conducted using Monte Carlo method (Efron and Tibshirani, 1986). In detail, modelled time series with the same structure as the original series were produced according to the frequency domain method of Ebisuzaki (1997). Then, correlation coefficients were computed between the modelled time series. The above processes were repeated 1000 times to obtain 1000 modelled correlation coefficients. The significance threshold was estimated based on the probability distribution of the modelled 1000 correlation coefficients. The procedure was performed using the algorithms of Macias-Fauria et al. (2012).

3. Results and Discussion

3.1. Stronger hydroclimatic signals derived from EWW

As shown in Fig. 3, the EWW chronologies generated using different detrending and standardization methods were significantly negatively correlated with Tmax, Tmean during May–June, and significantly positively correlated with Pre in May. In terms of the drought indices, all EWW chronologies were significantly positively correlated with the 1-month SPEI in May, 3-month SPEI during May–June, 12-month SPEI during May–October, and scPDSI during April–October. It can be found that EWW showed a much longer-term response to the multi-month SPEI and scPDSI than to precipitation after May. This may be because the summer temperatures still affected the soil water status as reflected by their negative correlations with EWW. Besides, soil has a memory effect on previous drought conditions, and this effect was considered by the multi-month SPEI and scPDSI (Vicente-Serrano et al., 2010a; Dai, 2011). The scPDSI had higher correlations with tree-ring width than the SPEI. This indicates that the scPDSI has a better ability than the SPEI in monitoring the influence of soil moisture status on tree growth in our sampling sites, and the reasons remain unknown. However, the significant correlations found between EWW and drought indices during autumn should not be regarded as a real drought impact, as the earlywood growth

7

would terminate in the mid- and late-growing season (Larson, 1969). For LWW, during the current growing season, the highest correlation was found between the NELR based LWW STD and July scPDSI ($r = 0.37$, $p < 0.01$), which was much lower than that found between the NELR based EWW STD and the July scPDSI ($r = 0.62$, $p < 0.01$), indicating that LWW had less sensitivity to the scPDSI. TRW generally exhibited the similar climate response as EWW but with relatively lower correlations.

5 Taking the NELR based STD chronologies as an example, the correlation coefficients between TRW and the monthly scPDSI from May to July were 0.59 ($p < 0.01$), 0.58 ($p < 0.01$), 0.58 ($p < 0.01$), respectively. However, for EWW, the correlation coefficients were 0.66 ($p < 0.01$), 0.66 ($p < 0.01$) and 0.62 ($p < 0.01$). The above response patterns were also revealed by the correlation coefficients between the prewhitened and linearly detrended series (Fig. 4), indicating that autocorrelations and secular trends in the tree-ring width chronologies and climate time series have limited effects on the relationships.

10 Significant climate-growth relationships were also observed prior to the current growing season. For example, most of EWW and LWW chronologies exhibited negative response to Tmax and Tmean during the late summer and early autumn of last year (Figs. 3–4). This may be ascribed that high temperatures in the late growing season of last year could enhance soil water evaporation, thus inducing moisture stress and limiting the accumulation of photosynthetic products for the next year tree-growth (Peng et al., 2014). The influence of moisture status prior to the current growing season can also be reflected by the

15 significant positive correlations between LWW and drought indices from September of two years earlier to May of last May. However, EWW had lower correlations with these monthly drought indices. A possible explanation may be that the interannual variations of EWW were mainly contributed by the moisture status of the growth year.

Since the impacts of scPDSI on tree-growth can last for several months, we analysed the responses of various tree-ring width parameters to the multi-month averaged scPDSI. The strongest climate-growth relationship was found between the NELR

20 based EWW STD chronology and the MJJ scPDSI ($r = 0.707$; $p < 0.01$; Fig. S6). Meanwhile, correlation coefficients derived from the methods SP67 and SPA50 were 0.67 ($p < 0.01$) and 0.68 ($p < 0.01$), respectively, which were lower than that based on NELR method (Fig. S6). This may be because the downward trend in MJJ scPDSI were better preserved using the NELR detrending method (Fig. S7). In addition, correlation coefficient between the NELR based EWW SSF chronology and the MJJ scPDSI was 0.705 ($p < 0.01$), which was quite close to that using the traditional STD method, indicating that the effects of so-

25 called "trend distortion" in our tree-ring series were limited.

We further tested the temporal stability and possible lags (leads) in the relationships between NELR based STD chronologies and the MJJ scPDSI on different frequency domain (Fig. 5). It can be found that EWW generally showed high degree of coherence with the MJJ scPDSI on all timescales (2- to 18-year) except the periodicities between 3.5- and 6.5-year. Different from EWW, LWW only varied in-phase with the MJJ scPDSI but with some lags during the period from 1970s to 1990s on

30 the timescales lower than 12-year. Moreover, LWW was inversely correlated with the MJJ scPDSI during the 1960s on the periodicities of 4- to 6-year. TRW showed an unstable relationship and certain lags to the MJJ scPDSI on the periodicities of 6- to 11-year. Therefore, it can be concluded that EWW has the most stable relationships with the MJJ scPDSI than LWW and TRW.

8

Previous studies based on TRW has evidenced that moisture status of the current growing season could strongly affect the radial growth of *P. tabulaeformis* (e.g. Cai and Liu, 2012; Cai et al., 2014; Cai et al., 2015; Chen et al., 2014; Fang et al., 2009; Fang et al., 2012b; Li et al., 2007; Liang et al., 2007; Liu et al., 2017; Song and Liu, 2011; Sun et al., 2012). Fast radial growth of *P. tabulaeformis* usually happens in the early growing season (Liang et al., 2009; Shi et al., 2008; Zeng et al., 2018). Increased water deficiency due to the rising temperature and inadequate rainfall in the early growing season could induce soil water deficiency thus suppressing cell expansion and cell growth in the cambium (Fritts, 1976), and resulting in the formation of narrow earlywood bands. The less sensitivity of LWW to moisture status of the current growing season may be ascribed to that the moisture restrictions on tree growth was alleviated in the rainy season (July–August; Fig. 2). Meanwhile, the response sensitivity of TRW to moisture status of the current growing season was not as strong as EWW, although they shared a similar climatic response pattern because EWW represents the majority of TRW (on average, the portion of EWW of TRW accounts for 65.8%).

3.2. MJJ scPDSI reconstruction using NELR based EWW STD chronology

Based on the above analyses, we selected the MJJ scPDSI as the target for hydroclimate reconstruction, and the NELR based EWW STD chronology as the predictor (Fig. 6a). The transfer function was estimated using a simple linear regression model as expressed in Eq. (2):

$$\text{MJJ scPDSI} = 4.74\text{EWW} - 4.32; (R^2 = 0.5, n = 53, p < 0.001), \qquad (2)$$

The model explains 50 % of the actual MJJ scPDSI variance over the period of 1953–2005. The calibration-verification tests show that r, R^2 and the sign-test are significant at the 0.01 level, and that RE and CE values are positive (Table 3). In addition, the p-value generated from DW and CS tests are larger than 0.05, indicating that there are no autocorrelations and long-term trends in the regression residuals (Table 3; Fig. 6). All test results confirm that the model is valid (Cook et al., 1999; Fritts, 1976).

Based on the above model, the MJJ scPDSI of the study region was reconstructed back to 1864 (Fig. 6c). We restored the variance of reconstruction to match the variance of instrumental MJJ scPDSI during the calibration period (1953–2005). Spatial correlation analysis indicates that the reconstruction most strongly represents Central China, including the western part of Henan, the northern part of Hubei, and the southern part of Shaanxi provinces (Fig. 1a).

3.3. Comparing the reconstructed MJJ scPDSI with other reconstructions and historical documents

On the interannual timescale (Figs. 7a–c), our reconstruction is significantly correlated with the $PDSI_{Cook}$ ($r = 0.36$; $p < 0.01$; 1864–2005), and Pre_{Chen} ($r = 0.45$; $p < 0.01$; 1864–2005). On the decadal and longer timescales, our reconstruction is significantly correlated with all other reconstructions (Figs. 7e–f). The common drought periods occurring in the 1870s and the 1920s were reflected in our reconstruction. These two drought periods were frequently observed in North and West China (Cai et al., 2014; Chen et al., 2014; Fang et al., 2012a; Kang et al., 2013; Liang et al., 2006; Liu et al., 2017; Zhang et al., 2017).

However, it should be noted that our reconstruction has some mismatches with others. On the interannual timescale, our reconstruction is not significantly correlated with the DWI_{Yang} over the whole period 1864–2000 ($r = –0.07$; $p = 0.5$; Fig. 7b). This probably due to the historical documents have limited ability in capturing the high frequency climatic variations (Zheng et al., 2014). On the decadal and longer timescales, our reconstruction varied out-of-phase with $PDSI_{Cook}$ during the period from the late 1940s to the early 1960s (Fig. 7d), weakly correlated with DWI_{Yang} after the 1940s (Fig. 7e), and leads Pre_{Chen} during the period of 1900s–1930s (Fig. 7f). The possible reasons might be that (1) the seasons that the three reconstructions aimed at are different from ours (June–August for $PDSI_{Cook}$, May–September for DWI_{Yang}, and April–June for Pre_{Chen} which is before the rainy season); (2) the DWI_{Yang} after the 1940s was calculated using instrumental May–September precipitation and the chronology of Chen et al. (2016b) also reflects precipitation, while the scPDSI is influenced not only by precipitation but also temperature and previous drought conditions; and (3) in the MADA network, there are still limited tree-ring sites around our sampling sites, which may cause some difference on local scale.

We also compared the dry and wet events derived from our reconstruction with those recorded in historical document records. The moderately to severely dry (wet) events are defined based on the scPDSI values less than –2 (larger than 2) according to Palmer (1965). It can be found that all the dry events and 70 % of the wet events can be verified by corresponding descriptions in historical documents (Table 4). While, there are still some mismatches between our reconstruction and the historical records. For example, no relevant document record is found for the year 1983 when an extreme wet event is shown in our reconstruction. In addition, some historical events are not reflected in our reconstruction, such as the wet event in 1963 and the dry event in 1942 (Wen, 2006). These mismatches may reflect the uncertainties of historical documents records and tree-ring.

3.4. Connections with EASMI

The reconstructed MJJ scPDSI and EASMI in general exhibit an in-phase relationship before the 1940s on the decadal and longer timescales (Fig. 8). This in-phase relationship was further verified found after conducting an 21-year moving window correlation analysis on the decadal-filtered scPDSI and EASMI (Fig. 9). As EASM direclty drives precipitation rather than the scPDSI, we compared the EASMI with the local precipitation (32°–34.5° N and 111°–112° E). It was found that the local precipitation also exhibit the similar variation as the scPDSI and EASMI before the 1940s (Fig. 9d). Therefore, the in-phase relationship between the decadal-filtered EASMI and scPDSI before the 1940s may be ascribed to the fact that a stronger EASM could induce enhanced local precipitation, thus increasing the soil moisture content.

Correlations between the decadal-filtered MJJ scPDSI and EASMI have decreased since the 1940s, and even became negative since the 1970s (Fig. 8; Fig. 9d). The direct cause might be that the in-phase relationship between the local precipitation and EASMI has been weaked since the 1950s, and even changed into anti-phase around the 1970s (Fig. 9d). The EASMI was designed to capture the leading mode of EASM precipitation variability, whose largest loading is in general located at the mei-yu/changma/baiu rainband (27.5°–32.5° N, 105°–120° E and 30°–37.5° N, 127.5°–150° E) (Zhao et al., 2015). The precipitation outside of this rainband could be in-phase, out-of-phase and uncorrelated with the mei-yu/changma/baiu rainfall due to the change of the leading mode of EASM precipitation (Wang et al., 2008), so its relationship with EASMI is unstable.

The EASM experienced an abrupt shift in the late 1970s, which caused a change of the leading mode of EASM precipitation (Wang, 2001; Ding et al., 2008). We demonstrated how this mode change affects the relationship between EASMI and precipitation in the eastern Qinling Mountains. As shown in Fig. 10a, the anomalies of the decadal-filtered MJJ precipitation exhibited similar variations over the Yangtzer River basin and Yellow-Huaihe River basins during 1901–1978, but they were divided by the Yangtze River, showing a dipole pattern during 1979–2005 (Fig. 10b). The south of the Yangtze River basin (27°–30° N) were the loading centres during both periods, and the decadal-filtered MJJ precipitation over this area were well captured by the designed EASMI as manifested by their significant positive correlations ($p < 0.1$) (Figs. 10c–d). On the contrary, the decadal-filtered MJJ precipitation over the north of the Yangtze River, including our sampling sites, varied out-of-phase with those over the south of the Yangtze River basin after the late 1970s, thus being negatively correlated with EASMI. In addition, it should also be noted that the decadal-filterd scPDSI was uncorrelated with precipitation since the 1940s. This weak relationship is similar to that found between the decadal-filterd scPDSI and DWI$_{Yang}$ (Fig. 9e), which may be ascribed to the combined influence of temperature and previous drought conditions. Therefore, the changing relationship between EASMI and local precipitation could not completely explain that between EASMI and scPDSI. These results suggest that we should take fully into account the complexity when evaluating the impact of EASM on the hydroclimatic conditions in the core region of EASM.

4. Conclusions

Besides TRW, climatic responses of EWW and LWW were also explored for the tree-ring samples of *P. tabulaeformis* in the eastern Qinling Mountains (Central China). Regardless of the detrending and standardisation methods used, the resulting EWW chronologies are more sensitive to early summer soil moisture conditions than LWW and TRW during the instrumental period 1953–2005. The MJJ scPDSI (1864–2005) reconstructed from the NELR based EWW STD chronology captures the past early summer hydroclimatic fluctuations, further validated by other proxy-based reconstructions and historical document records in adjacent regions. Moreover, the reconstruction shows a stable relationship with the EASMI before the 1940s on the decadal and longer timescales. This indicates that EWW has great potentials to reconstruct early summer hydroclimatic conditions in this area. Our finding in this study is different from that found at a well-drained site in South China, where strongest moisture signals were contained in LWW with a different tree species (Zhao et al., 2017a, b). Therefore, more EWW and LWW related studies should be conducted in terms of tree species differences, different environmental condition, etc., in humid and semi-humid regions of China, that provides a possibility to understand EASM variations at longer time periods beyond the meteorological records.

11

Data availability

The tree-ring data used in this study are available on request (shijf@nju.edu.cn). DWI, precipitation reconstruction, and dry/wet events recorded in historical documents are available from corresponding authors or publications. MADA is available from https://www.ncdc.noaa.gov/paleo-search/study/10435. The 200 hPa zonal wind dataset of NOAA-20c is available from https://www.esrl.noaa.gov/psd/data/gridded/data.20thC_ReanV2c.html. The gridded scPDSI dataset CRU scPDSI 3.25 is available from https://crudata.uea.ac.uk/cru/data/drought/. The gridded precipitation dataset GPCC v7 is available from ftp://ftp.dwd.de/pub/data/gpcc/html/fulldata_v7_doi_download.html.

Author contributions

YZ and JS designed the study. JS provided the tree-ring samples. YZ performed tree-ring width measurement, data analyses and interpretation. JS, SS, XS and HL assisted in data interpretation. YZ wrote the first draft of the paper. All authors revised the paper.

Competing interests

The authors declare that they have no conflict of interest.

Acknowledgments

References

Akaike, H.: A new look at the statistical model identification, IEEE T. Automat. Contr., 19, 716–723, https://doi.org/10.1109/TAC.1974.1100705, 1974.

Beguería, S., and Vicente-Serrano, S. M.: Calculation of the Standardised Precipitation-Evapotranspiration Index. R Package version 1.7, https://cran.r-project.org/web/packages/SPEI/index.html, 2012.

Cai, Q., and Liu, Y.: Climatic response of Chinese pine and PDSI variability in the middle Taihang Mountains, north China since 1873, Trees, 27, 419–427, https://doi.org/10.1007/s00468-012-0812-6, 2012.

Cai, Q., Liu, Y., Lei, Y., Bao, G., and Sun, B.: Reconstruction of the March-August PDSI since 1703 AD based on tree rings of Chinese pine (*Pinus tabulaeformis* Carr.) in the Lingkong Mountain, southeast Chinese Loess Plateau, Clim. Past, 10, 509–521, https://doi.org/10.5194/cp-10-509-2014, 2014.

Cai, Q., Liu, Y., Liu, H., and Ren, J.: Reconstruction of drought variability in North China and its association with sea surface temperature in the joining area of Asia and Indian–Pacific Ocean, Palaeogeogr. Palaeoclimatol. Palaeoecol., 417, 554–560, https://doi.org/10.1016/j.palaeo.2014.10.021, 2015.

Cai, Q., Liu, Y., Liu, H., Sun, C., and Wang, Y.: Growing-season precipitation since 1872 in the coastal area of subtropical southeast China reconstructed from tree rings and its relationship with the East Asian summer monsoon system, Ecol. Indic., 82, 441–450, https://doi.org/10.1016/j.ecolind.2017.07.012, 2017.

Chen, F., Yuan, Y., Wei, W., Yu, S., Fan, Z., Zhang, R., Zhang, T., and Shang, H.: Tree-ring-based reconstruction of precipitation in the Changling Mountains, China, since A.D.1691, Int. J. Biometeorol., 56, 765–774, https://doi.org/10.1007/s00484-011-0431-8, 2012.

Chen, F., Yuan, Y., Zhang, R., and Qin, L.: A tree-ring based drought reconstruction (AD 1760–2010) for the Loess Plateau and its possible driving mechanisms, Global Planet. Change, 122, 82–88, https://doi.org/10.1016/j.gloplacha.2014.08.008, 2014.

Chen, F., Yu, S., Yuan, Y., Wang, H., and Gagen, M.: A tree-ring width based drought reconstruction for southeastern China: links to Pacific Ocean climate variability, Boreas, 45, 335–346, https://doi.org/10.1111/bor.12158, 2016a.

Chen, F., Zhang, R., Wang, H., Qin, L., and Yuan, Y.: Updated precipitation reconstruction (AD 1482–2012) for Huashan, north-central China, Theor. Appl. Climatol., 123, 723–732, https://doi.org/10.1007/s00704-015-1387-0, 2016b.

Chen, X., and Xu, L.: Temperature controls on the spatial pattern of tree phenology in China's temperate zone, Agr. Forest Meteorol., 154–155, 195– 202, https://doi.org/10.1016/j.agrformet.2011.11.006, 2012.

Chinese Academy of Meteorological Sciences (Eds.): Yearly charts of dryness/wetness in China for the last 500-year period, China Cartographic Publishing House, Beijing, China, 1981 (in Chinese).

Compo, G. P., Whitaker, J. S., Sardeshmukh, P. D., Matsui, N., Allan, R. J., Yin, X., Gleason, B. E., Vose, R. S., Rutledge, G., Bessemoulin, P., Brönnimann, S., Brunet, M., Crouthamel, R. I., Grant, A. N., Groisman, P. Y., Jones, P. D., Kruk, M. C., Kruger, A. C., Marshall, G. J., Maugeri, M., Mok, H. Y., Nordli, Ø., Ross, T. F., Trigo, R. M., Wang, X. L., Woodruff, S. D., and Worley, S. J.: The Twentieth Century Reanalysis Project, Quarterly J. Roy. Meteorol. Soc., 137, 1–28, https://doi.org/10.1002/qj.776, 2011.

Cook, E. R., Briffa, K. R., Shiyatov, S. G., & Mazepa, V.: Tree-ring standardization and growth-trend estimation, in: Methods of dendrochronology: Applications in the environmental sciences, edited by E. R. Cook & L. A. Kairiukstis., Kluwer Academic Publishers, Dordrecht, Netherlands, 104–123, http:/.doi.org/10.1007/978-94-015-7879-0, 1990.

Cook, E. R., Meko, D. M., Stahle, D. W., and Cleaveland, M. K.: Drought reconstructions for the continental United States, J. Climate, 12, 1145–1162, 1999.

Cook, E. R., Anchukaitis, K. J., Buckley, B. M., D'Arrigo, R. D., Jacoby, G. C., and Wright, W. E.: Asian monsoon failure and megadrought during the last millennium, Science, 328, 486–489, https://doi.org/10.1126/science.1185188, 2010.

Cox, D. R., and Stuart, A.: Some quick sign tests for trend in location and dispersion, Biometrika, 42, 80–95, https://doi.org/10.2307/2333424, 1955.

Dai, A.: Characteristics and trends in various forms of the Palmer Drought Severity Index during 1900–2008, J. Geophys. Res., 116, D12115, https://doi.org/10.1029/2010JD015541, 2011.

Ding, Y., and Dai, X.: Temperature variation in China during the last 100 years, Meteorological Monthly, 20, 19–26, 1994 (in Chinese).

Ding, Y., Wang, Z., and Sun, Y.: Inter-decadal variation of the summer precipitation in East China and its association with decreasing Asian summer monsoon. Part I: Observed evidences, Int. J. Climatol., 28, 1139–1161, https://doi.org/10.1002/joc.1615, 2008.

Ding, Y., Sun, Y., Liu, Y., Si, D., Wang, Z., Zhu, Y., Liu, Y., Song, Y., and Zhang, J.: Interdecadal and interannual variabilities of the Asian summer monsoon and its projection of future change, Chinese J. Atmos. Sci., 37, 253–280, https://doi.org/10.3878/j.issn.1006-9895.2012.12302, 2013 (in Chinese).

Durbin, J., and Watson, G. S.: Testing for serial correlation on least squares regression: I, Biometrika, 37, 409–428 https://doi.org/10.2307/2332391, 1950.

Ebisuzaki, W.: A method to estimate the statistical significance of a correlation when the data are serially correlated, J. Climate, 10, 2147–2153, https://doi.org/10.1175/1520-0442(1997)010<2147:AMTETS>2.0.CO;2, 1997.

Efron, B., and Tibshirani, R.: Bootstrap methods for standard errors, confidence intervals, and other measures of statistical accuracy, Stat. Sci., 1, 54–77, 1986.

Fan, Z.-X., Bräuning, A., and Cao, K.-F.: Tree-ring based drought reconstruction in the central Hengduan Mountains region (China) since A.D. 1655, Int. J. Climatol., 28, 1879–1887, https://doi.org/10.1002/joc.1689, 2008.

Fang, K., Gou, X., Chen, F., D'Arrigo, R., and Li, J.: Tree-ring based drought reconstruction for the Guiqing Mountain (China): linkages to the Indian and Pacific Oceans, Int. J. Climatol., 30, 1137–1145, https://doi.org/10.1002/joc.1974, 2009.

Fang, K., Gou, X., Chen, F., Li, J., D'Arrigo, R., Cook, E., Yang, T., and Davi, N.: Reconstructed droughts for the southeastern Tibetan Plateau over the past 568 years and its linkages to the Pacific and Atlantic Ocean climate variability, Clim. Dynam., 35, 577–585, https://doi.org/10.1007/s00382-009-0636-2, 2010.

Fang, K., Gou, X., Chen, F., Frank, D., Liu, C., Li, J., and Kazmer, M.: Precipitation variability during the past 400 years in the Xiaolong Mountain (central China) inferred from tree rings, Clim. Dynam., 39, 1697–1707, https://doi.org/10.1007/s00382-012-1371-7, 2012a.

Fang, K., Gou, X., Chen, F., Liu, C., Davi, N., Li, J., Zhao, Z., and Li, Y.: Tree-ring based reconstruction of drought variability (1615–2009) in the Kongtong Mountain area, northern China, Global Planet. Change, 80–81, 190–197, https://doi.org/10.1016/j.gloplacha.2011.10.009, 2012b.

Fritts, H. C.: Tree rings and climate, Academic Press, New York, 567 pp., 1976.

Gou, X., Yang, T., Gao, L., Deng, Y., Yang, M., and Chen, F.: A 457-year reconstruction of precipitation in the southeastern Qinghai-Tibet Plateau, China using tree-ring records, Chinese Sci. Bull., 58, 1107–1114, https://doi.org/10.1007/s11434-012-5539-7, 2013.

Grinsted, A., Moore, J. C., and Jevrejeva, S.: Application of the cross wavelet transform and wavelet coherence to geophysical time series, Nonlinear Proc. Geoph., 11, 561–566, https://doi.org/10.5194/npg-11-561-2004, 2004.

He, H. W.: The great North-China drought famine of the early Guangxu reign (1876–1879), The Chinese University Press, Hong Kong, 1980 (in Chinese).

Hughes, M. K., Wu, X. D., Shao, X. M., and Garfin, G. M.: A preliminary reconstruction of rainfall in North-Central China since A.D. 1600 from tree-ring density and width, Quaternary Res., 42, 88–99, https://doi.org/10.1006/qres.1994.1056, 1994.

Jones, P., and Hulme, M.: Calculating regional climatic time series for temperature and precipitation: methods and illustrations, Int. J. Climatol., 16, 361–377, https://doi.org/10.1002/(SICI)1097-0088(199604)16:4<361::AID-JOC53>3.0.CO;2-F, 1996.

Kang, S., Yang, B., Qin, C., Wang, J., Shi, F., and Liu, J.: Extreme drought events in the years 1877–1878, and 1928, in the southeast Qilian Mountains and the air–sea coupling system, Quatern. Int., 283, 85–92, https://doi.org/10.1016/j.quaint.2012.03.011, 2013.

Knapp, P. A., Maxwell, J. T., and Soulé, P. T.: Tropical cyclone rainfall variability in coastal North Carolina derived from longleaf pine (*Pinus palustris* Mill.): AD 1771–2014, Climatic Change, 135, 311–323, https://doi.org/10.1007/s10584-015-1560-6, 2016.

Larson, P. R.: Wood formation and the concept of wood quality, Yale University: School of Forestry Bulletin, 74, 1–54, 1969.

14

Lei, Y., Liu, Y., Song, H., and Sun, B.: A wetness index derived from tree-rings in the Mt. Yishan area of China since 1755 AD and its agricultural implications, Chinese Sci. Bull., 59, 3449–3456, https://doi.org/10.1007/s11434-014-0410-7, 2014.

Li, J., Chen, F., Cook, E. R., Gou, X., and Zhang, Y.: Drought reconstruction for North Central China from tree rings: the value of the Palmer drought severity index, Int. J. Climatol., 27, 903–909, https://doi.org/10.1002/joc.1450, 2007.

5   Li, J., Shi, J., Zhang, D. D., Yang, B., Fang, K., and Yue, P. H.: Moisture increase in response to high-altitude warming evidenced by tree-rings on the southeastern Tibetan Plateau, Clim. Dynam., 48, 649–660, https://doi.org/10.1007/s00382-016-3101-z, 2016.

Li, Y., Fang, K., Cao, C., Li, D., Zhou, F., Dong, Z., Zhang, Y., and Gan, Z.: A tree-ring chronology spanning the past 210 years in the coastal area of Southeast China and its relationship with climate change, Clim. Res., 67, 209–220,
10   https://doi.org/10.3354/cr01376, 2016.

Liang, E., and Eckstein, D.: Light rings in Chinese pine (*Pinus tabulaeformis*) in semiarid areas of north China and their palaeo-climatological potential, New Phytol., 171, 783–791, https://doi.org/10.1111/j.1469-8137.2006.01775.x, 2006.

Liang, E., Liu, X., Yuan, Y., Qin, N., Fang, X., Huang, L., Zhu, H., Wang, L., and Shao, X.: The 1920s drought recorded by tree rings and historical documents in the semi-arid and arid areas of Northern China, Climatic Change, 79, 403–432,
15   https://doi.org/10.1007/s10584-006-9082-x, 2006.

Liang, E., Shao, X., Liu, H., and Eckstein, D.: Tree-ring based PDSI reconstruction since AD 1842 in the Ortindag Sand Land, east Inner Mongolia, Chinese Sci. Bull., 52, 2715–2721, https://doi.org/10.1007/s11434-007-0351-5, 2007.

Liang, E., Eckstein, D., and Shao, X.: Seasonal cambial activity of relict Chinese Pine at the northern limit of its natural distribution in North China - exploratory results, IAWA J., 30, 371–378, 2009.

20   Liu, H., Shao, X., and Huang, L.: Reconstruction of early-summer drought indices in mid-north region of China after 1500 using tree ring chronologies, Quaternary Sciences, 22, 220–229, 2002 (in Chinese).

Liu, X., Nie, Y., and Wen, F.: Seasonal dynamics of stem radial increment of *Pinus taiwanensis* Hayata and its response to environmental factors in the Lushan Mountains, Southeastern China, Forests, 9, 387, https://doi.org/10.3390/f9070387, 2018a.

Liu, Y., Zhang, X., Song, H., Cai, Q., Li, Q., Zhao, B., Liu, H., and Mei, R.: Tree-ring-width-based PDSI reconstruction for
25   central Inner Mongolia, China over the past 333 years, Clim. Dynam., 48, 867–879, https://doi.org/10.1007/s00382-016-3115-6, 2017.

Liu, Y., Song, H., Sun, C., Song, Y., Cai, Q., Liu, R., Lei, Y., and Li, Q.: The 600-mm precipitation isoline distinguishes tree-ring width responses to climate in China, Natl. Sci. Rev., https://doi.org/10.1093/nsr/nwy101, 2018b.

Macias-Fauria, M., Grinsted, A., Helama, S., and Holopainen, J.: Persistence matters: Estimation of the statistical significance
30   of paleoclimatic reconstruction statistics from autocorrelated time series, Dendrochronologia, 30, 179–187, https://doi.org/10.1016/j.dendro.2011.08.003, 2012.

Mann, M. E.: Smoothing of climate time series revisited, Geophys. Res. Lett., 35, L16708, https://doi.org/10.1029/2008gl034716, 2008.

Meko, D., and Graybill, D. A.: Tree-ring reconstruction of upper Gila River discharge, Water Resour. Bull., 31, 605–616,
35   https://doi.org/10.1111/j.1752-1688.1995.tb03388.x, 1995.

Melvin, T. M., Briffa, K. R., Nicolussi, K., and Grabner, M.: Time-varying-response smoothing, Dendrochronologia, 25, 65–69, https://doi.org/10.1016/j.dendro.2007.01.004, 2007.

Melvin, T. M., and Briffa, K. R.: A "signal-free" approach to dendroclimatic standardisation, Dendrochronologia, 26, 71–86, https://doi.org/10.1016/j.dendro.2007.12.001, 2008.

40   Osborn, T. J., Briffa, K. R., and Jones, P. D.: Adjusting variance for sample-size in tree ring chronologies and other regional-mean time-series, Dendrochronologia, 15, 89–99, 1997.

15

Palmer, W. C., Meteorological drought, U.S. Department of Commerce, Weather Bureau Research Paper 45, 58 pp., 1965.

Peng, J., Liu, Y., and Wang, T.: A tree-ring record of 1920's—1940's droughts and mechanism analyses in Henan Province, Acta Ecologica Sinica, 34, 3509–3518, https://doi.org/10.5846/stxb201306121687, 2014.

Schneider, U., Becker, A., Finger, P., Meyer-Christoffer, A., Rudolf, B., and Ziese, M.: GPCC full data monthly product version 7.0 at 0.5°: Monthly land-surface precipitation from rain-gauges built on GTS-based and historic data, https://doi.org/10.5676/DWD_GPCC/FD_M_V7_050, 2015.

Shi, J.F., Liu, Y., Vaganov, E. V., Li, J. B., Cai, Q. F.: Statistical and process-based modeling anlyses of tree growth response to climate in semi-arid area of north central China: A case study of *Pinus tabulaeformis*, J. Geophys. Res., 113, G01026, https://doi.org/10.1029/2007JG000547, 2008

Shi, J., Li, J., Cook, E. R., Zhang, X., and Lu, H.: Growth response of *Pinus tabulaeformis* to climate along an elevation gradient in the eastern Qinling Mountains, central China, Clim. Res., 53, 157–167, https://doi.org/10.3354/cr01098, 2012.

Shi, J., Lu, H., Li, J., Shi, S., Hou, X., and Li, L.: Tree-ring based February–April precipitation reconstruction for the lower reaches of the Yangtze River, Southeast China, Global Planet. Change, 131, 82–88, https://doi.org/10.1016/j.gloplacha.2015.05.006, 2015.

Song, H., and Liu, Y.: PDSI variations at Kongtong Mountain, China, inferred from a 283-year *Pinus tabulaeformis* ring width chronology, J. Geophys. Res.-Atmos., 116, https://doi.org/10.1029/2011jd016220, 2011.

Stahle, D. W., Cleaveland, M. K., Fye, F. K., Burnette, D. J., Grissino-Mayer, H. D., Therrell, M. D., Griffin, R. D., Meko, D. M., and Villanueva Diaz, J.: Cool- and warm-season precipitation reconstructions over western New Mexico, J. Climate, 22, 3729–3750, https://doi.org/10.1175/2008JCLI2752.1, 2009.

Sun, J., Liu, Y., Sun, B., and Wang, R.: Tree-ring based PDSI reconstruction since 1853 AD in the source of the Fenhe river basin, Shanxi province, China, Sci. China Earth Sci., 55, 1847–1854, https://doi.org/10.1007/s11430-012-4369-4, 2012.

van der Schrier, G., Barichivich, J., Briffa, K. R., and Jones, P. D.: A scPDSI-based global data set of dry and wet spells for 1901-2009, J. Geophys. Res.-Atmos., 118, 4025–4048, https://doi.org/10.1002/jgrd.50355, 2013.

Vicente-Serrano, S. M., S. Beguería, and J. I. López-Moreno, A multi-scalar drought index sensitive to global warming: The Standardized Precipitation Evapotranspiration Index–SPEI, J. Climate, 23, 1696–1718, doi:10.1175/2009JCLI2909.1, 2010.

Wang, B., Wu, Z., Li, J., Liu, J., Chang, C.-P., Ding, Y., and Wu, G.: How to measure the strength of the East Asian Summer Monsoon, J. Climate, 21, 4449–4463, https://doi.org/10.1175/2008jcli2183.1, 2008.

Wang, D., and Wang, A.: Applicability assessment of GPCC and CRU precipitation products in China during 1901 to 2013, Climatic and Environmental Research, 22, 446–462, https://doi.org/10.3878/j.issn.1006-9585.2016.16122, 2017 (in Chinese).

Wang, H.: The weaking of the Aisan Monsoon Circulation after the end of 1970's, Advances in Atmospheric Sciences, 18, 376–386, https://doi.org/10.1007/BF02919316, 2001.

Wang, L., Fang, K., Chen, D., Dong, Z., Zhou, F., Li, Y., Zhang, P., Ou, T., Guo, G., Cao, X., and Yu, M.: Intensified variability of the El Niño-Southern Oscillation enhances its modulations on tree growths in southeastern China over the past 218 years, Int. J. Climatol., 38, 5293–5304, https://doi.org/10.1002/joc.5730, 2018.

Wells, N., Goddard, S., and Hayes, M. J.: A self-calibrating Palmer Drought Severity Index, J. Climate, 17, 2335–2351, https://doi.org/10.1175/1520-0442(2004)017<2335:ASPDSI>2.0.CO;2, 2004.

Wen, K.: Meteorological disasters in China, China Meteorological Press, Beijing, China, 2006 (in Chinese).

Wigley, T. M. L., Briffa, K. R., and Jones, P. D.: On the average value of correlated time series, with applications in dendroclimatology and hydrometeorology, J. Clim. App. Meteorol., 23, 201–213, https://doi.org/10.1175/1520-0450(1984)023<0201:otavoc>2.0.co;2, 1984.

16

Xu, H., Sun, Z., Guo, G., and Feng, L.: Geographic distribution of *Pinus tabulaeformis* Carr. and classification of provenance regions, Scientia Silvae Sinicae, 17, 258–270, 1981 (in Chinese).

Yang, B., Kang, S., Ljungqvist, F. C., He, M., Zhao, Y., and Qin, C.: Drought variability at the northern fringe of the Asian summer monsoon region over the past millennia, Clim. Dynam., 43, 845–859, https://doi.org/10.1007/s00382-013-1962-y, 2013a.

Yang, F., Shi, F., Kang, S., Wang, S., Xiao, Z., Nakatsuka, T., and Shi, J.: Comparison of the dryness/wetness index in China with the Monsoon Asia Drought Atlas, Theor. Appl. Climatol., 114, 553–566, https://doi.org/10.1007/s00704-013-0858-4, 2013b.

Zeng, Q., Rossi, S., and Yang, B.: Effects of age and size on xylem phenology in two conifers of Northwestern China, Front. Plant. Sci., 8, 2264, https://doi.org/10.3389/fpls.2017.02264, 2018.

Zhang, Y., Zheng, H., Long, R., and Yang, B.: Seasonal cambial activity and formation of phloem and xylem in in eight forest tree species grown in North China, Scientia Silvae Sinicae, 18, 366–379, 1982 (in Chinese).

Zhang, Y., Tian, Q., Guillet, S., and Stoffel, M.: 500-yr. precipitation variability in Southern Taihang Mountains, China, and its linkages to ENSO and PDO, Climatic Change, 144, 419–432, https://doi.org/10.1007/s10584-016-1695-0, 2017.

Zheng, J., Ge, Q., Hao, Z., Liu, H., Man, Z., Hou, Y., Fang, X.,: Paleoclimatology proxy recorded in historical documents and method for reconstruction on climate change, Quaternary Sciences, 34, 1186–1196, doi: 10.3969/j.issn.1001-7410.2014.06.07, 2014 (in Chinese).

Zhao, G., Huang, G., Wu, R., Tao, W., Gong, H., Qu, X., and Hu, K.: A new upper-level circulation index for the East Asian Summer Monsoon variability, J. Climate, 28, 9977–9996, https://doi.org/10.1175/jcli-d-15-0272.1, 2015.

Zhao, Y., Shi, J., Shi, S., Wang, B., and Yu, J.: Summer climate implications of tree-ring latewood width: a case study of *Tsuga longibracteata* in South China, Asian Geographer, 34, 131–146, https://doi.org/10.1080/10225706.2017.1377623, 2017a.

Zhao, Y., Shi, J., Shi, S., Yu, J., and Lu, H.: Tree-ring latewood width based July–August SPEI reconstruction in South China since 1888 and its possible connection with ENSO, J. Meteorol. Res.-PRC, 31, 39–48, https://doi.org/10.1007/s13351-017-6096-4, 2017b.

17

Table 1. Characteristics of climate data.

Climate data	Source	Longitude (° E)	Latitude (° N)	Elevation (m a.s.l.)	Temporal cover
Tmax, Tmean, Tmin, Pre	Luanchuan (LC) meteorological station	111.6	33.8	751	1957–2005
	Xixia (XX) meteorological station	111.5	33.3	250	1957–2005
	Ruyang (RY) meteorological station	112.5	34.2	311	1957–2005
	Nanzhao (NZ) meteorogical station	112.6	33.6	198	1956–2005
scPDSI	CRU scPDSI 3.25 (van der Schrier et al., 2013)	111–112	32–34.5	—	1953–2005
SPEI	Calculated in R using the SPEI package with the Tmax, Tmin and Pre data (Beguería and Vicente-Serrano 2012)	—	—	—	1957–2005

Table 2. Long-term hydroclimatic reconstructions and East Aisan Summer Monsoon index (EASMI) selected for comparion with the reconstructed MJJ scPDSI.

Time series	Source	Longitude (° E)	Latitude (° N)	Temporal cover
June–August PDSI	Monsoon Asia Drought Atlas (MADA, Cook et al., 2010)	111.25	33.75	1864–2005
April–June precipitation in Mount Huashan (HS)	Chen et al., 2016	110.08	34.48	1864–2005
Dryness/wetness index (DWI)	Yang et al., 2013b	111.25	33.75	1864–2000
EAMSI	Calculated using the 200 hPa zonal wind anomalies (NOAA-20c; Compo et al., 2011) according to the definition of Zhao et al. (2015)	—	—	1864–2005

19

Table 3. Statistics for split calibration-verification of the regression model.

Calibration period	r	R^2	DW value (p-value)	CS p-value	Verification period	RE	CE	Sign-test
Full period (1953–2005)	0.71**	0.50**	2.03 (0.53)	0.85	—	—	—	—
Early half (1953–1979)	0.68**	0.46**	2.02 (0.49)	1	Late half (1979–2005)	0.53	0.53	22+/5–**
Late half (1979–2005)	0.73**	0.54**	2.02 (0.50)	1	Early half (1953–1979)	0.46	0.45	21+/6–**

** $p < 0.01$; r, Pearson correlation coefficient; R^2, explained variance; DW, Durbin-Watson test; CS, Cox and Stuart trend test; RE, reduction of error; and CE, coefficient of efficiency.

Calibration period	r	R^2	DW value (p-value)	CS p-value	Verification period	RE	CE	Sign-test

Table 4. Moderately to severely dry (scPDSI $\leqslant$ –2) and wet (scPDSI $\geqslant$ 2) events derived from the MJJ scPDSI reconstruction and corresponding descriptions from historical documents.

Event type	Year	scPDSI	Description
	1879	–3.61	A mega-drought occurred has caused a great famine over Henan, Shaanxi and other provinces in North China in the early Guangxu reign (1876–1879)[a]
	1900	–2.24	Severe drought from spring to Autumn over Henan and Shaanxi
	1923	–2.28	Drought over Henan and Shaanxi
Dry	1926	–2.33	No harvest at Ruyang (West Henan) due to severe drought
	1929	–2.53	Summer drought over Henan and Shaanxi
	1994	–2.12	Severe drought occurred in April, May and July over west Henan
	1995	–2.10	Intensified drought severity since April 22 over Henan
	2000	–2.94	The drought from Feburary to May is the worst one since 1950 over Henan
	1864	2.94	Not available
	1869	2.31	Flood in summer and autumn over Henan
	1883	2.62	Persistent rainfall in summer at Shanxian and Mianchi (Northwest Henan)
	1885	3.07	Flood in summer at Lingbao and Shanxian (Northwest Henan)
Wet	1894	3.06	Not available
	1895	2.11	Flood over the Qinhe River (Northwest Henan) in summer
	1898	3.77	Severe flood in summer at Lushi (Northwest Henan), Shangnan (Southeast Shaanxi) and Danjiang (Northwest Hubei)

21

1905	2.26	Persistent rainfall in spring and summer over Henan
1906	3.65	Heavy rainfall in summer over Henan
1910	2.05	Flood in summer and autumn over Henan
1911	3.84	Heavy rainfall in summer over Henan
1912	2.01	Heavy rainfall and flood in summer over Nanyang (Southwest Henan)
1933	2.51	Heavy rainfall in summer over Henan and Shaanxi
1934	3.11	Summer rainfall over Henan, South Shaanxi and Northwest Hubei
1936	3.72	Not available
1944	2.38	Flood over Henan; Rainstorm in Zhenan (Southeast Shannxi) on July 8; The Tianhui Channel (Southeast Shaanxi) was destroyed by flood on May 13
1948	2.81	Wheat loss caused by summer rainfall
1949	2.95	Not available
1973	2.97	Not available
1980	2.07	Rainfall in June is higher than usual for most regions over Henan
1983	4.15	Not available
1984	2.33	From June to September, there are 5 large-scale rainstorms over Henan
1990	2.32	Not available

[a] Historical description of the 1879 drought event is cited from He (1980), and others from Wen (2006)
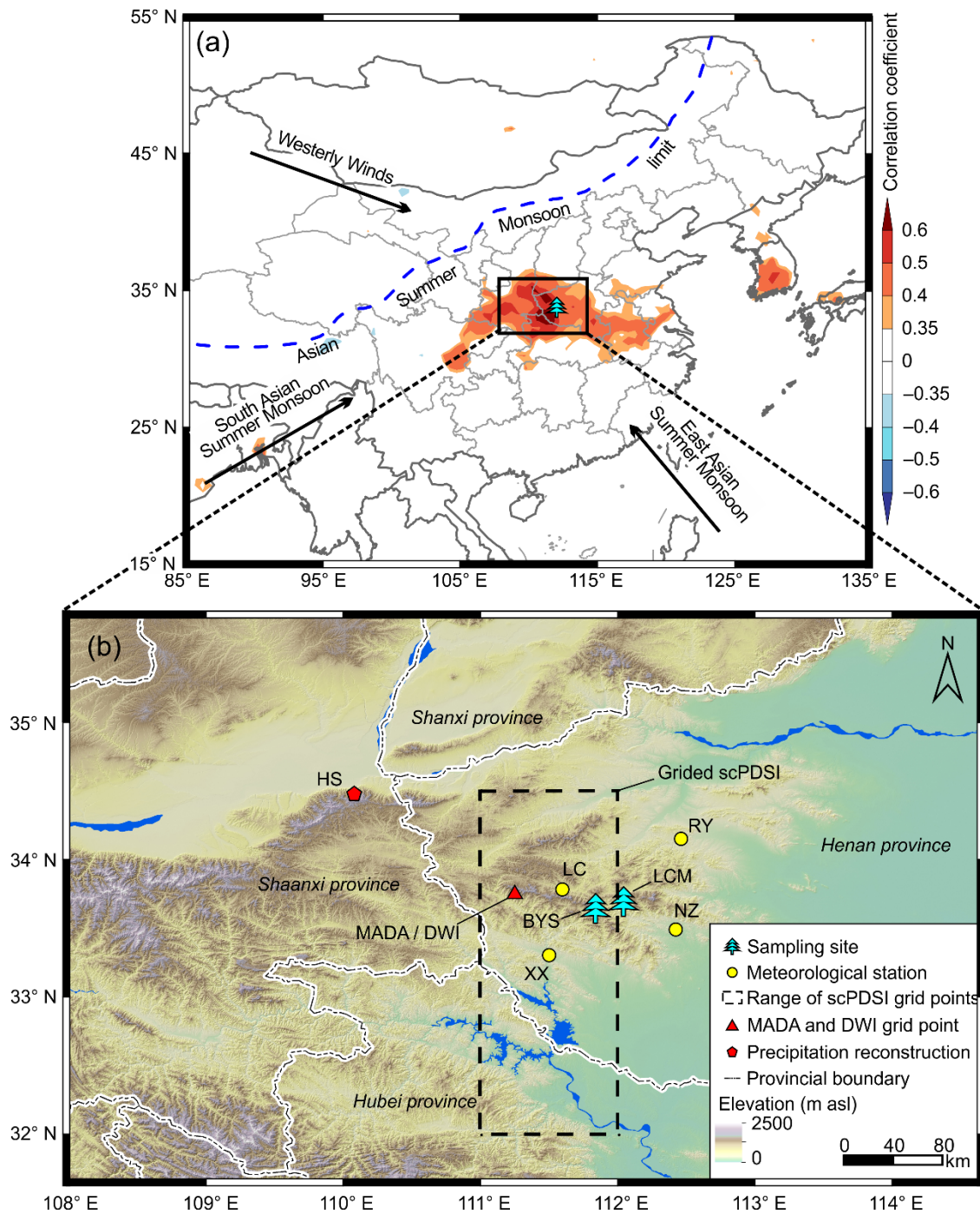
Figure 1. Map of the study region. **(a)** Location of the sampling site (tree symbol), and the spatial correlations between the May–July (MJJ) scPDSI reconstruction and the gridded scPDSI dataset (van der Schrier et al., 2013) during the period 1953–2005. The color bar indicates the correlation coefficient. The blue dashed line indicates the Asian Summer Monsoon limit

(Yang et al., 2013a). **(b)** The circles indicate the locations of the four meteorological stations (LC: Luanchuan, XX: Xixia, RY: Ruyang, and NZ: Nanzhao). The triangle indicates the location of selected grid data from the datasets Monsoon Asia Drought Atlas (MADA; Cook et al., 2010) and Dryness/Wetness Index (DWI; Yang et al., 2013b). The pentagon indicates a tree-ring width based precipitation reconstruction in Huashan Mount (HS, Chen et al., 2016b). The dashed rectangle indicates the gridded scPDSI obtained from the gridded scPDSI dataset (van der Schrier et al., 2013).

5
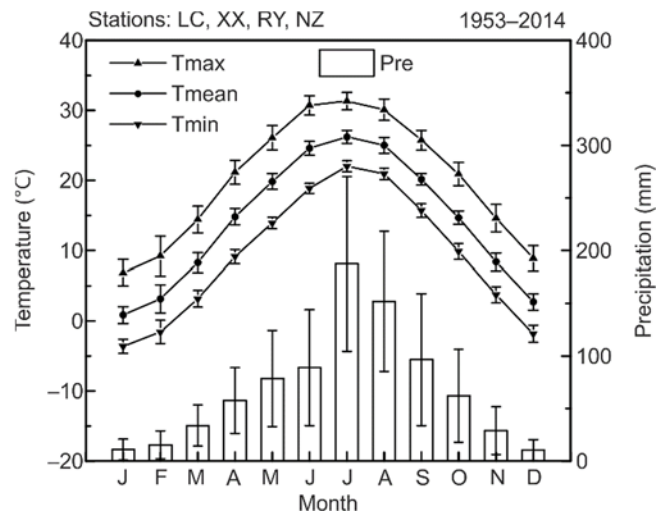
Figure 2. Monthly maximum, mean, minimum temperature (Tmax, Tmean, Tmin), and total precipitation (Pre) averaged from the four selected meteorological stations (LC, XX, RY, NZ) during the period 1953–2005. Error bar denote ± one standard deviation.

5
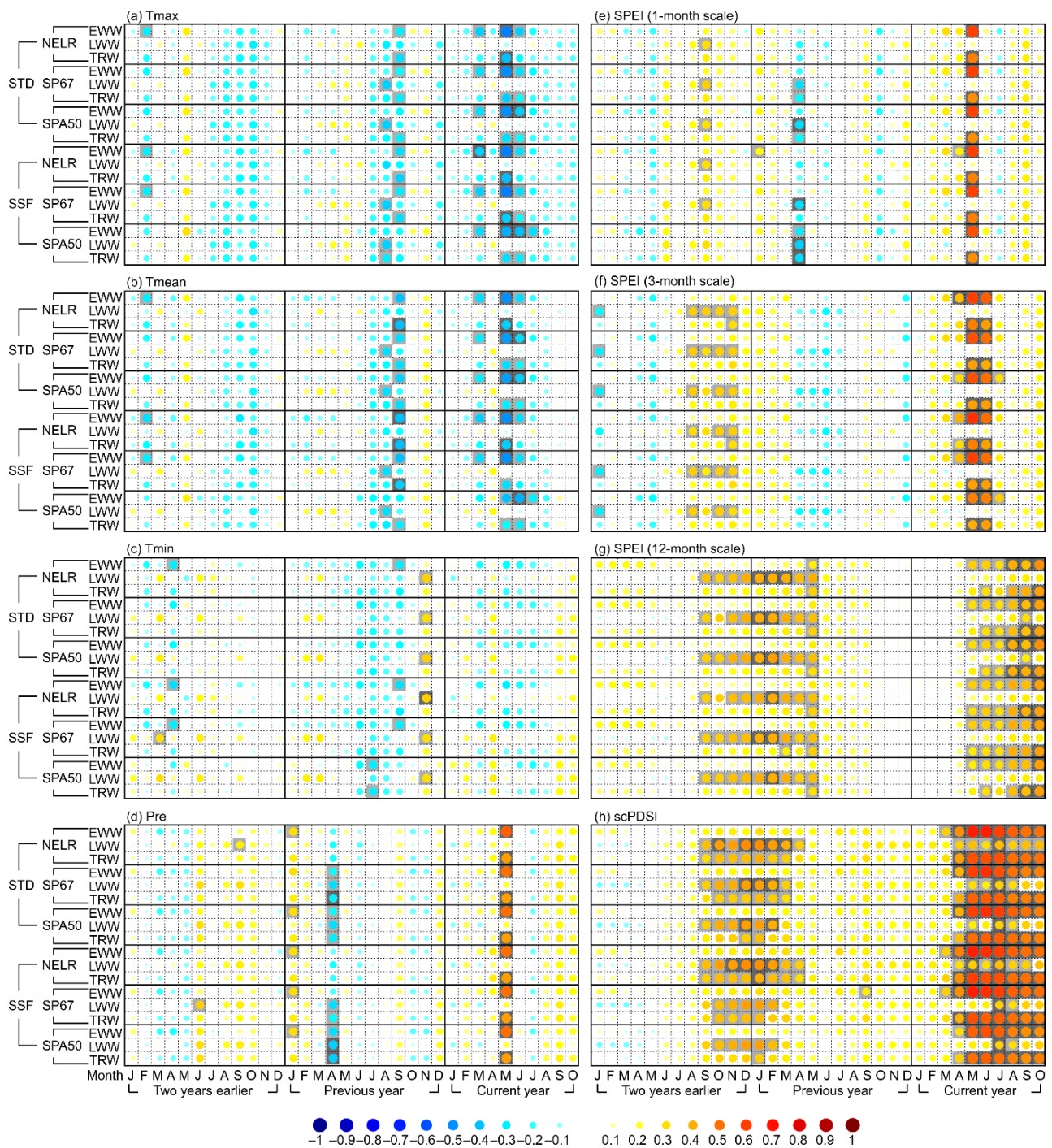
Figure 3. Matrix plots for the correlation coefficients between tree-ring width chronologies and monthly climate time series

from January of two years earlier to October of the current year. The climatic factors are monthly **(a)** maximum temperature

(Tmax), **(b)** mean temperature (Tmean), **(c)** minimum temperature (Tmin), **(d)** total precipitation (Pre), **(e)** SPEI of 1-month scale, **(f)** SPEI of 3-month scale, **(g)** SPEI of 12-month scale, and **(h)** scPDSI. EWW, LWW, and TRW indicate the earlywood width, latewood width, and total tree-ring width, respectively. NELR, SP67, and SPA50 indicate the three detrending methods: (1) negative exponential function together with linear regression with negative (or zero) slope (NELR), (2) cubic smoothed splines with a 50 % frequency cutoff of 67 % of the series length (SP67), and (3) age-dependent splines with an initial stiffness of 50 years (SPA50). STD and SSF indicate the two standardization methods "standard" and "signal-free", respectively. The correlation coefficients are reflected by the colorful and different-size circles, which can be referred to the color bar as shown at the bottom of the figure. The squares filled with light and dark gray color indicate that the correlation coefficients are statistically significant at the 0.05 and 0.01 level, which are tested using the Monte Carlo method (Efron and Tibshirani, 1986; Macias-Fauria et al., 2012).
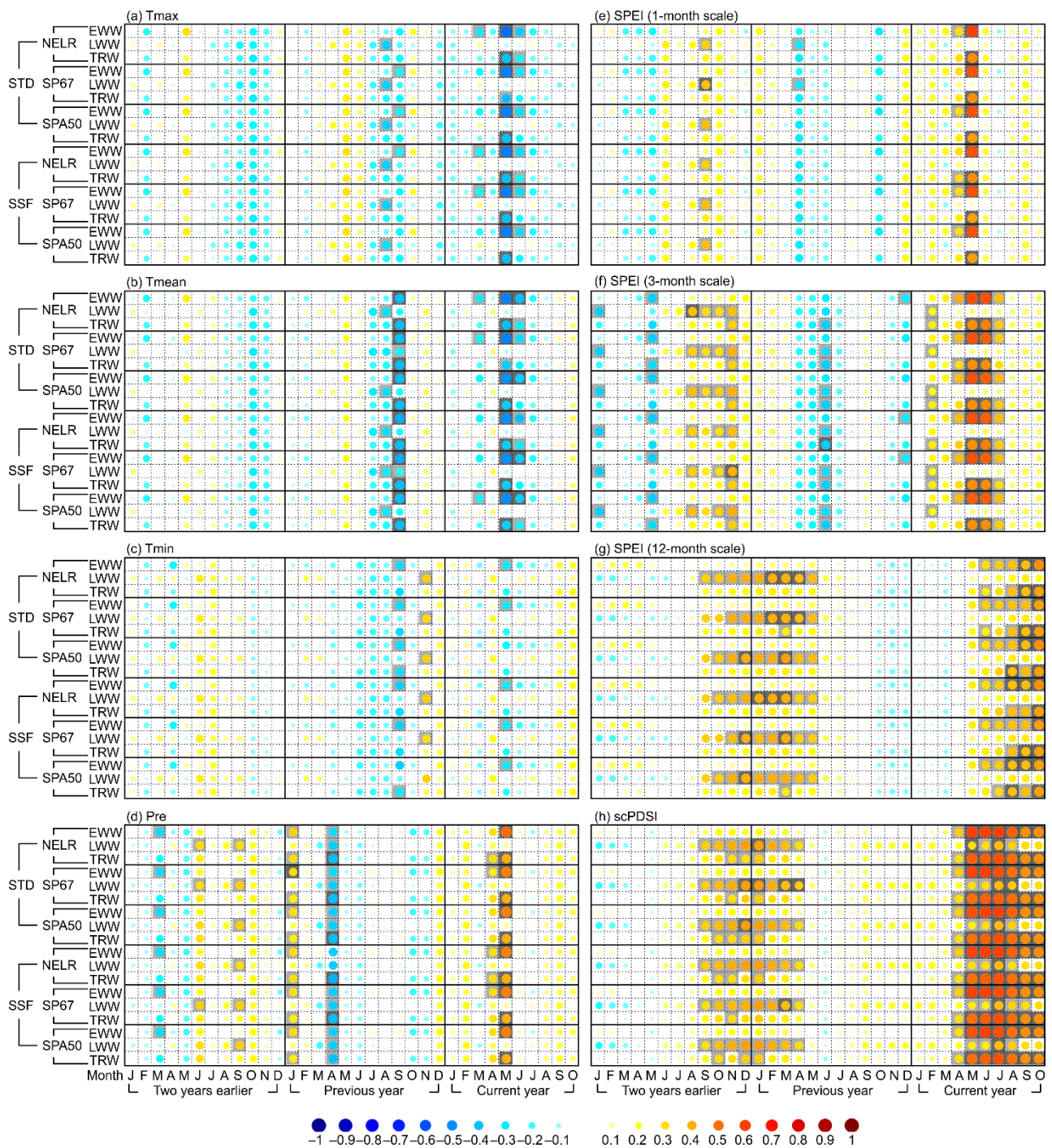
Figure 4. Correlation coefficients between the prewhitened and linearly detrended tree-ring width chronologies and climate time series. The explanations and legends are the same as Figure 3.
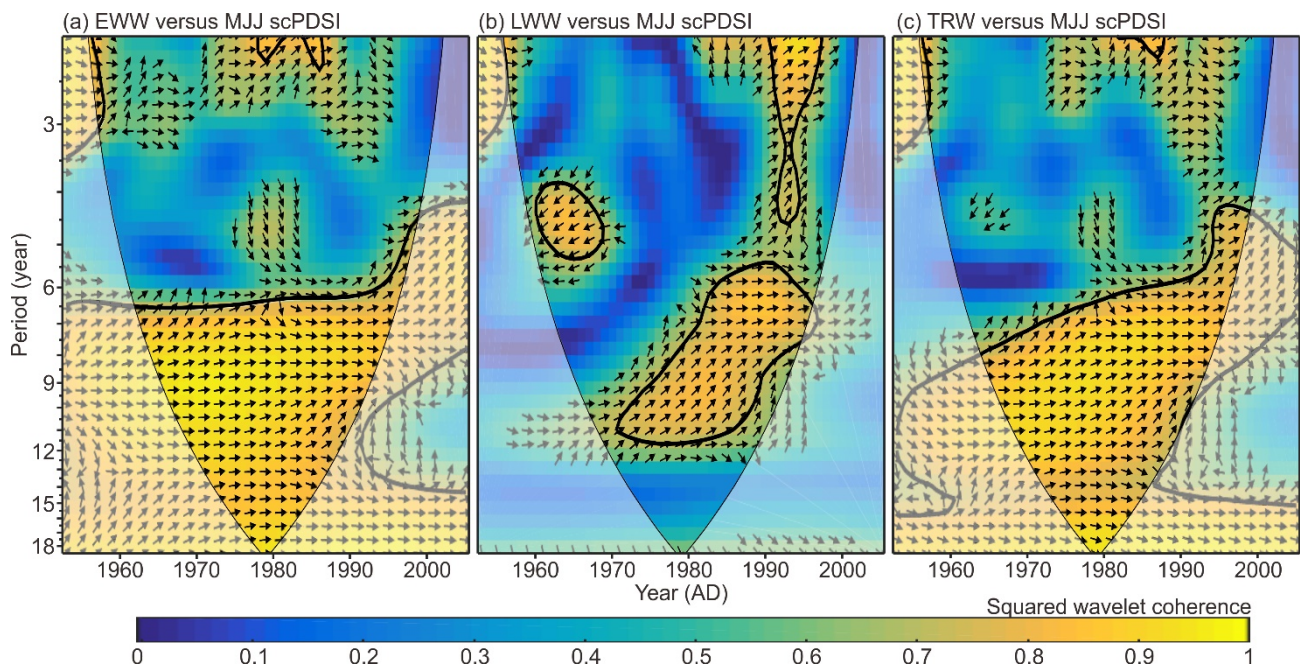
Figure 5. Squared wavelet coherence and phase relationship between the NELR based tree ring-width STD chronologies and MJJ scPDSI. **(a–c)** represent the results for EWW, LWW, and TRW, respectively. The color bar indicates the squared wavelet coherence. The arrows indicate the phase relationship with in-phase (anti-phase) pointing right (left), and MJJ scPDSI leading (lagging) tree-ring width with 90° pointing straight up (down). The thick contour indicates the 5% significance level against red noise. The cone of influence (COI) where edge effects might distort the picture is shown as a lighter shade.
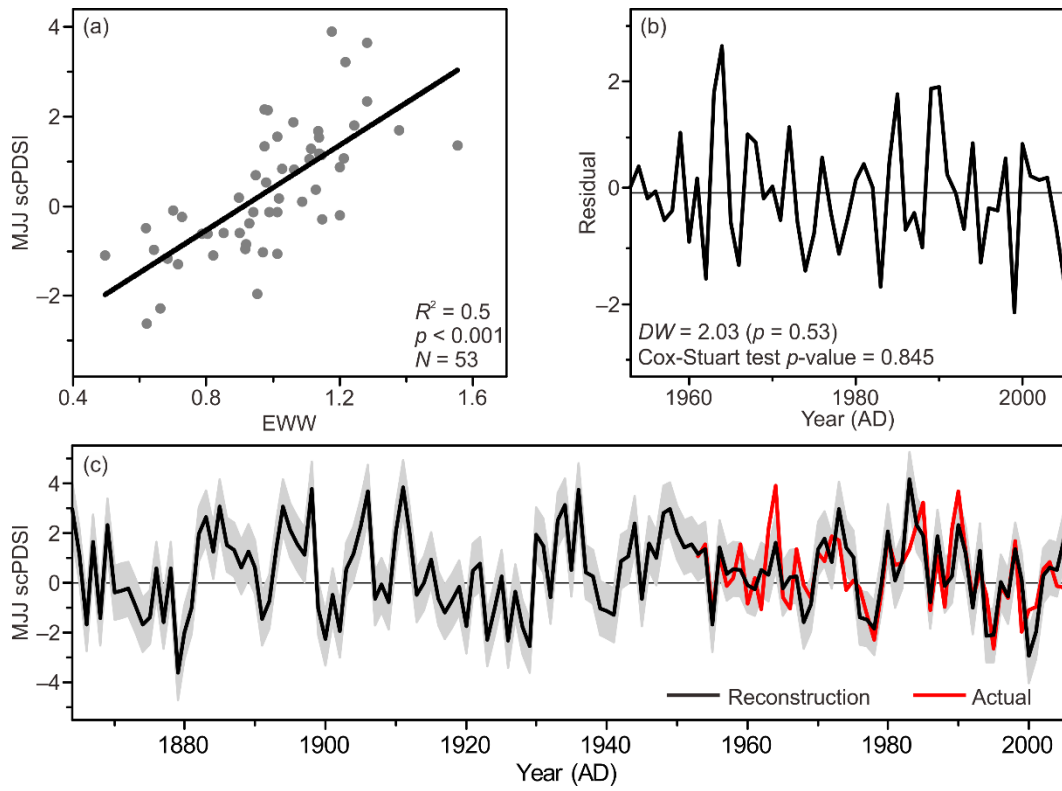
Figure 6. MJJ scPDSI reconstruction using NELR based EWW STD chronology. **(a)** Scatter diagram during the period 1953–2005, and **(b)** the resulting residuals. **(c)** MJJ scPDSI reconstruction (black line, after variance adjusted) and instrumental MJJ scPDSI (red line). Shade area denotes the uncertainties of reconstruction in the form of ± 1 root mean square error.
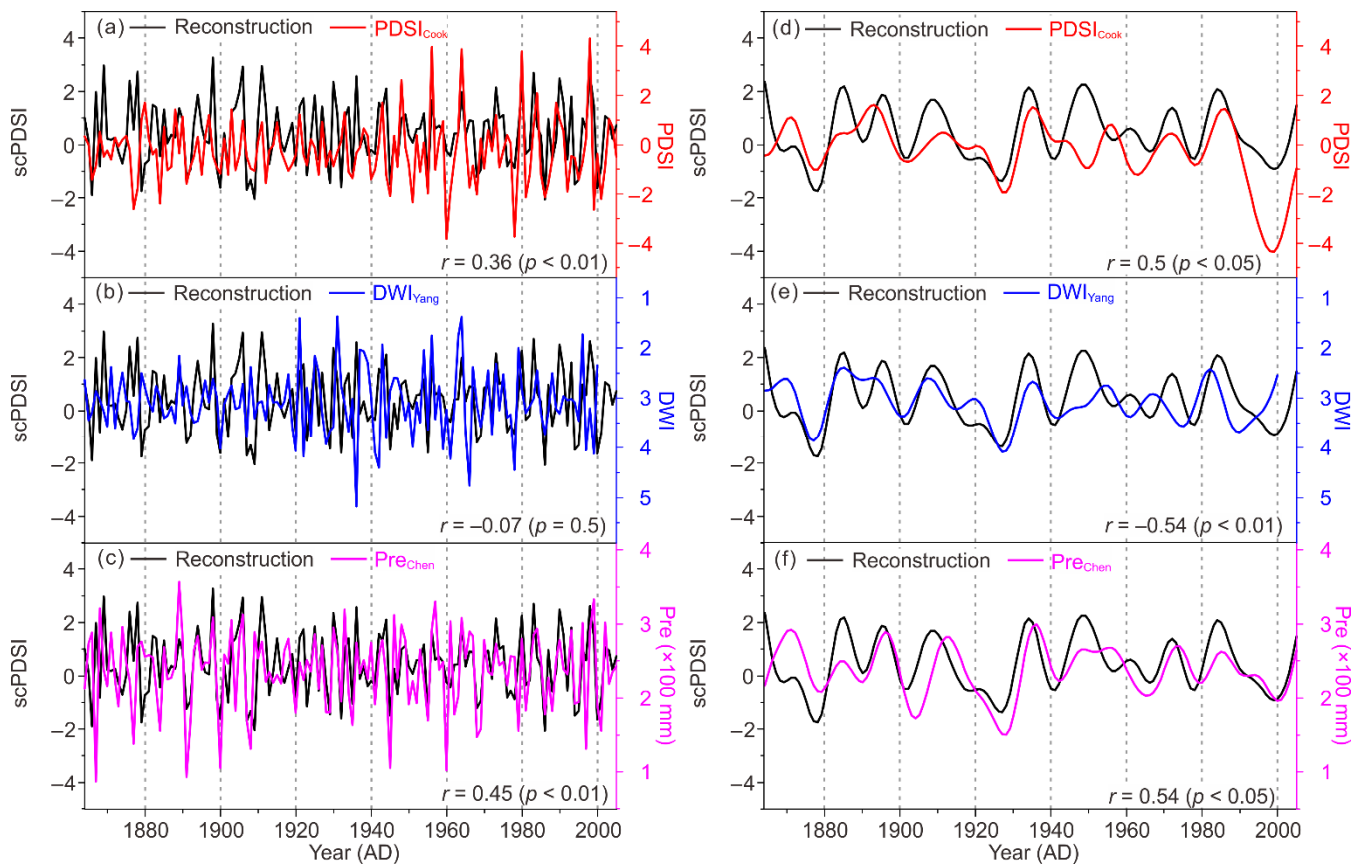
Figure 7. Comparison of the reconstructed MJJ scPDSI (black line) with other hydroclimatic reconstructions in adjacent regions on the interannual (left panels), and decadal and longer timescales (right panels). The referenced reconstructions are **(a, d)** June–August PDSI of MADA NO. 370 point (Cook et al., 2010), **(b, e)** reversed DWI (Yang et al., 2013b), and **(c, f)** TRW based April–June precipitation (Pre) reconstruction (Chen et al., 2016b). The interannual and decadal and longer fluctuations were separated using the adaptive 10 point "Butterworth" low-pass filter with 0.1 cutoff frequency (Mann, 2008). r represents the Pearson correlation coefficient between the reconstructed MJJ scPDSI and other hydroclimatic reconstruction over their common period. The significance level for all correlation coefficients were tested using the Monte Carlo method (Efron and Tibshirani, 1986; Macias-Fauria et al., 2012).
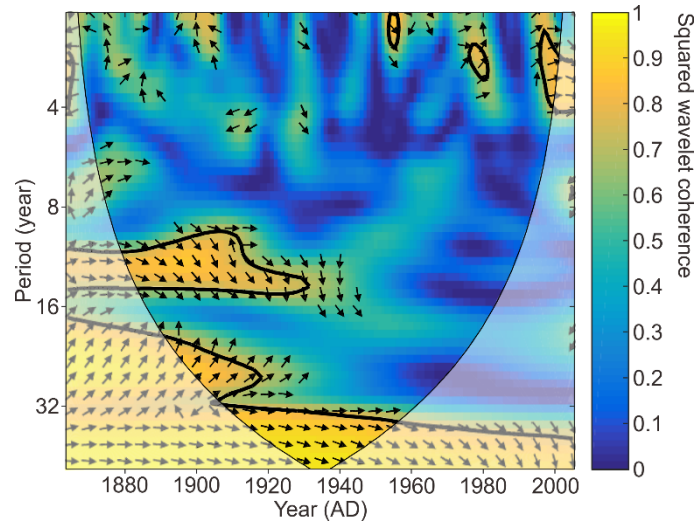
Figure 8. Squared wavelet coherence and phase relationship between the reconstructed MJJ scPDSI and EASMI (Zhao et al., 2015). The color bar indicates the squared wavelet coherence. The arrows indicate the phase relationship with in-phase (anti-phase) pointing right (left), and EASM leading (lagging) scPDSI with 90° pointing straight up (down). The thick contour indicates the 5 % significance level against red noise. The cone of influence (COI) where edge effects might distort the picture is shown as a lighter shade.
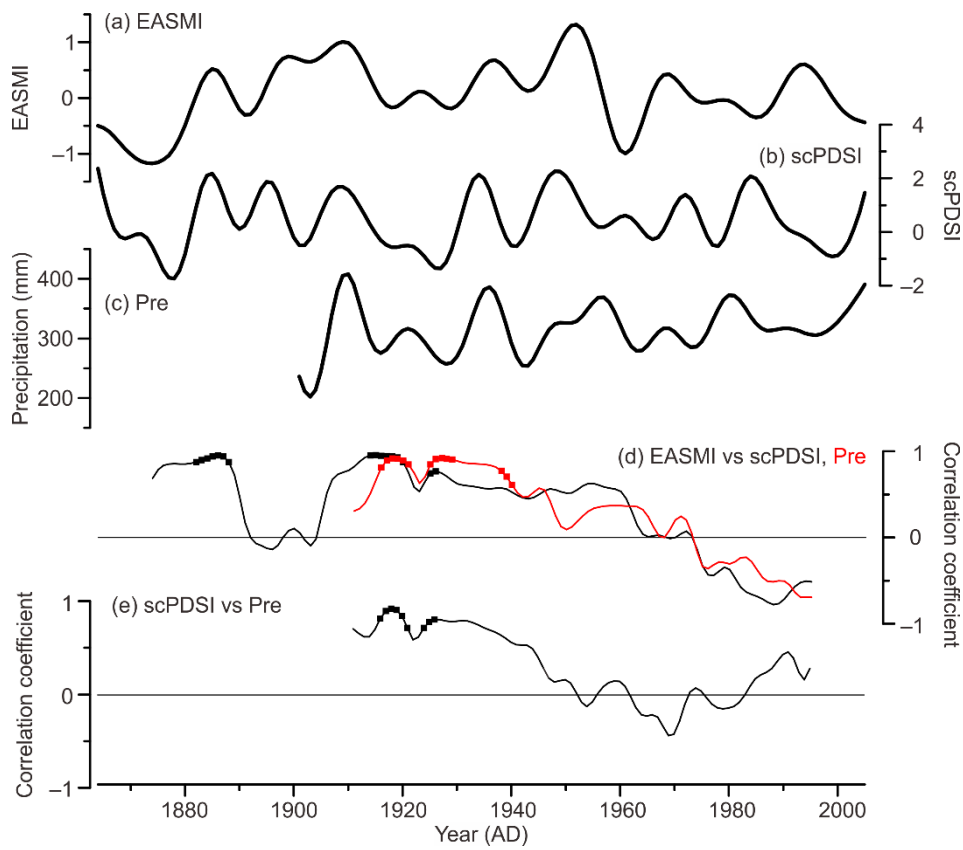
Figure 9. Comparison between the decadal and longer fluctuations of May–July **(a)** EASMI (Zhao et al., 2017), **(b)** reconstructed scPDSI, and **(c)** precipitation (Pre) over the reconstructed area (GPCC v7; Schneider et al., 2015). **(d)** 21-year moving Pearson correlation coefficients between the decadal-filtered EASMI and scPDSI (black), and Pre (red). **(e)** 21-year moving Pearson correlations between the decadal filtered scPDSI and Pre (black). The decadal and longer fluctuations were derived using the adaptive 10 point "Butterworth" low-pass filter with 0.1 cutoff frequency (Mann, 2008). Statistically significant ($p < 0.05$) correlations are denoted as squares, which were tested using the the Monte Carlo method (Efron and Tibshirani, 1986; Macias-Fauria et al., 2012).
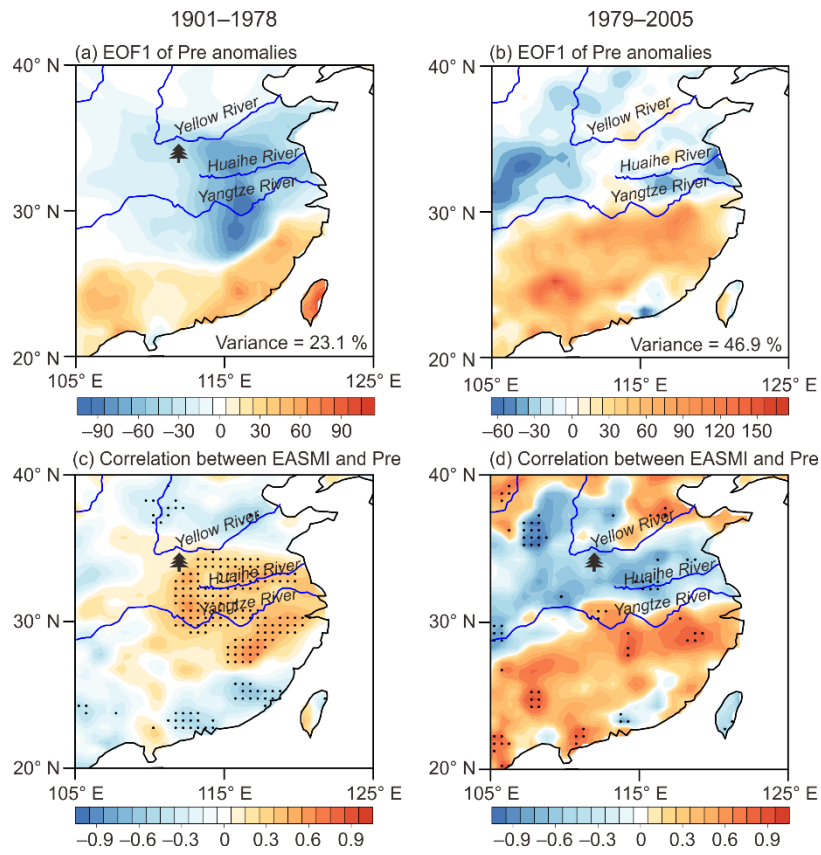
Figure 10. (a–b) The leading empirical orthogonal function (EOF) modes of decadal filtered May–July GPCC precipitation anomalies for the periods 1901–1978 (left panel) and 1979–2005 (right panel). The color bar indicates the EOF values. **(c–d)** Spatial correlations between the decadal filtered May–July EASMI defined by Zhao et al. (2015) and precipitation (Pre) for the periods 1901–1978 (left panel) and 1979–2005 (right panel). The color bar indicates the correlation coefficient. The dot indicates that the correlation is statistically significant ($p < 0.1$), which was tested using the Monte Carlo method (Efron and Tibshirani, 1986; Macias-Fauria et al., 2012). The decadal and longer fluctuations of precipitation were derived using the adaptive 10 point "Butterworth" low-pass filter with 0.1 cutoff frequency (Mann, 2008). The tree symbol denotes the study region.